Multiscale three-dimensional CFD modeling for PECVD of amorphous silicon thin films

Marquis Crose[a], Weiqi Zhang[a], Anh Tran[a], Panagiotis D. Christofides[a,b,*]

[a] Department of Chemical and Biomolecular Engineering, University of California, Los Angeles, CA 90095, USA
[b] Department of Electrical and Computer Engineering, University of California, Los Angeles, CA 90095, USA

A B S T R A C T

The development of a three-dimensional, multiscale computational fluid dynamics (CFD) model is presented here which aims to capture the deposition of amorphous silicon thin films via plasma-enhanced chemical vapor deposition (PECVD). The macroscopic reactor scale and the microscopic thin film growth domains which define the multiscale model are linked using a dynamic boundary which is updated at the completion of each time step. A novel parallel processing scheme built around a message passing interface (MPI) structure, in conjunction with a distributed collection of kinetic Monte Carlo algorithms, is applied in order to allow for transient simulations to be conducted using a mesh with greater than 1.5 million cells. Due to the frequent issue of thickness non-uniformity in thin film production, an improved PECVD reactor design is proposed. The resulting geometry is shown to reduce the product offset from $\sim 25\,nm$ to less than $13\,nm$ using identical deposition parameters.

© 2018 Elsevier Ltd. All rights reserved.

1. Introduction

The past two decades have seen continual development in the multiscale modeling of plasma-enhanced chemical vapor deposition (PECVD) with specific applications to the manufacturing of silicon thin films for use in the photovoltaic and microelectronics industries (e.g., Collins et al. (1994); da Silva and Morimoto (2002); Rasoulian and Ricardez-Sandoval (2015)). Accurate modeling of thin film deposition remains a key element in the effort to improve product quality and to cut down on manufacturing costs due to the difficulties associated with continuous and/or in situ measurements during chambered deposition processes (Economou et al., 1989; Rasoulian and Ricardez-Sandoval, 2014; 2015). Recently, Crose et al. (2017b) demonstrated a novel multiscale computational fluid dynamics (CFD) model, which combined a macroscopic CFD domain with a microscopic surface domain through a common boundary which lies on the surface of the silicon wafer. Although advanced modeling of chemical reactors via CFD has existed for some time (Gerogiorgis and Ydstie, 2005), the work of Crose et al. (2015) was the first to capture the link between PECVD reactor behavior and the microscopic domain. In particular, non-uniform deposition of *a*-Si:H (amorphous silicon) films was studied and provided a basis for future multiscale CFD modeling endeavors. Nonetheless, the two-dimensional axisymmetric nature of the model limits the exploration of some phenomena which exist in the three-dimensional in space process. Specifically, two-dimensional (2D) axisymmetric models cannot represent the full geometry of showerhead holes that provide reactant gases to the plasma region – a key feature when considering the uniformity of thin film products.

Given the aforementioned motivations, the framework previously developed for use in 2D applications is extended here to the three dimensional in space domain. Using a three-dimensional (3D) rendering which captures the typical geometry of chambered, parallel-plate PECVD reactors, a CFD model is proposed in the present work which is capable of reproducing accurately both plasma chemistry and fluid flow into the reaction zone through the showerhead region. With regard to the microscopic domain (i.e., the surface of the silicon wafer), a detailed kinetic Monte Carlo (kMC) algorithm developed previously by Crose et al. (2017b) is applied in order to capture both the exchange of mass and energy, as well as the microstructure of the a-Si:H thin film. Given that the startup and operation of PECVD reactors are inherently dynamic, the proposed simulations cannot derive accurate reactor behavior from steady-state solutions; however, the computationally demanding nature of the transient simulations necessitates the use of a parallel computation strategy as well as taking advantage of multiple-time-scale phenomena occurring in the process. In this work, a Message Passing Interface (MPI) structure is
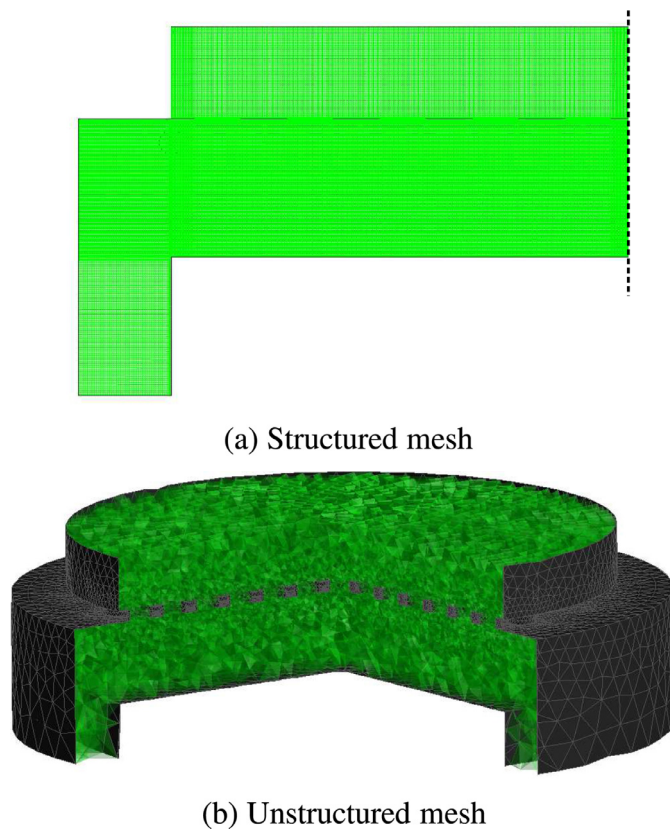
(a) Structured mesh

(b) Unstructured mesh

Fig. 1. (a) 2D axisymmetric geometry after discretization using a structured mesh containing 120,000 cells. (b) Collection of 1.5 million polygons which define the unstructured, 3D mesh.

adopted which allows for the discretization of both the macroscopic CFD volume and the microscopic kMC algorithm. The outlined multiscale model including its parallel implementation is applied to the deposition of 300 nm thick a-Si:H thin films revealing significant non-uniformities in the thickness of the thin film product. An improved reactor geometry is proposed which utilizes a polar showerhead arrangement and a radially-adjusted showerhead hole diameter. This geometry is shown to reduce thickness non-uniformity in the *a*-Si:H thin film product from ∼8% to less than 4%, representing significant product quality improvement and financial savings.

2. Three-dimensional modeling

Recently, Crose et al. (2017b) demonstrated the need for multiscale modeling in the PECVD process due to the interconnection between the macroscopic, reactor scale and the microscopic, thin film growth domains. Specifically, a two-dimensional (2D) axisymmetric geometry was used in the creation of the reactor mesh and a hybrid kinetic Monte Carlo (kMC) algorithm was applied to capture the growth of amorphous silicon (*a*-Si:H) thin film layers. The common boundary between the reactor mesh and microscopic model is of key importance as it allows for the distinct domains to remain linked throughout the course of transient simulations, and will be discussed at length in the multiscale workflow section. Although this model has proved useful in designing optimized reactor operational strategies, some features of the PECVD reactor are lost when using 2D representations. In looking at Fig. 1a and 1b, the difference between showerhead geometries becomes clear: the cylindrical showerhead holes and their associated spatial arrangement of the 3D system cannot be directly translated to 2D models.

Given the primary motivation of addressing *a*-Si:H thin film product quality (in particular, thin film spatial non-uniformity) through improved PECVD reactor design, in this work the development of a 3D multiscale CFD model will be presented including both the macroscopic and microscopic domains, as well as the associated dynamic boundary conditions and parallel computing implementation.

2.1. CFD geometry and meshing

As discussed previously, we utilize a 3D, cylindrical PECVD reactor geometry (see Fig. 1b) with dimensions typical of those used in industry. The showerhead holes, visible in Figs. 1b and 14 a, have a diameter of 1 cm and are evenly spaced in a rectangular array throughout the inlet region. In order to solve the partial differential equations which capture the gas phase mass, momentum and energy balances, the reactor geometry is discretized using an unstructured mesh containing ∼1.5 million tetrahedral cells. While previous efforts in modeling PECVD systems have relied on structured meshing (e.g., Crose et al. (2017b)) due to the possibility for higher mesh quality, in terms of orthogonality and aspect ratio, these models were based on 2D geometries with rectangular structures; however, in this work the curvature of the cylindrical reactor shell and showerhead holes favor the use of unstructured mesh compositions.

Specifically, the reactor mesh is built from a collection of tetrahedral cells with non-uniform cell density. Regions in which significant gradients are expected in temperature, species concentration, flow velocity, etc. (i.e., near walls, corners and highly curved surfaces) have been given higher cell density as opposed to the bulk fluid regions, see Fig. 1b. In order to obtain industrially relevant plasma distributions and thin film growth, accurate flow modeling of the process gas throughout the chamber is paramount. As an additional consideration, the cell density near surfaces is directly correlated to the flow characteristics of the gas, and in particular, the boundary layer which is formed at the interface of the fluid and solid phases. Given the relatively low flow rate of process gas (75 SCCM) and low chamber pressure (1 Torr), flow along the surface of the wafer is expected to be laminar (note: preliminary results from the macroscopic model and earlier work suggest a Reynold's number of Re = 2.28×10^{-4}). As a result, the mesh density directly above the substrate surface has been tuned such that the boundary layer may be captured within one cell 'layer' to provide accurate predictions necessary for the linked microscopic model. Although the choice to use an unstructured mesh in this manner rather than a simplified structured mesh comes at the cost of computational efficiency, the ease in designing new reactor geometries without constraints for showerhead hole size and curvature necessitates its use and the associated computational demands will be discussed at length in the parallel programming section below.

It is important to note that throughout this work ANSYS software is applied to the creation of the geometric mesh (specifically, ICEM meshing) and as a solver for the PDEs describing transport phenomena and chemical reactions (ANSYS Inc., 2013). The ANSYS Fluent software alone cannot yield a multiscale model for the PECVD process of interest; consequently, three user defined functions (UDFs) have been developed to tailor the solver to the deposition of *a*-Si:H thin films. More specifically, the thirty four most dominant gas phase reactions have been accounted for via a volumetric reaction scheme which includes terms for the nine primary plasma reactions which lead to thin film growth. The necessary electron density within the plasma region is calculated using a product of the zero-order Bessel function and a sine function which account for the spatial dependencies within the cylindrical reaction zone. The third UDF necessary to the multiscale nature of the model simulates the growth of *a*-Si:H thin films along the
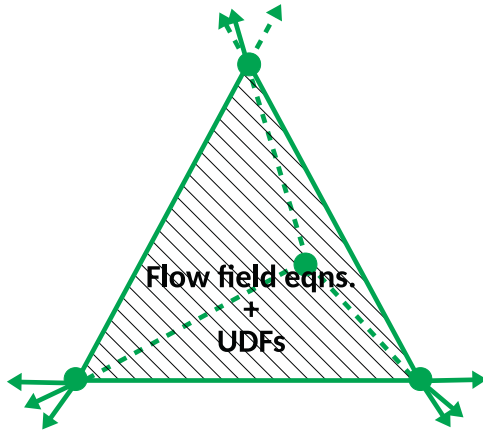
Fig. 2. Individual unit cell within the unstructured mesh.

surface of the wafer substrate. The details of these UDFs, in particular the kinetic Monte Carlo (kMC) algorithm which defines the microscopic domain, are expanded upon at length in the following sections.

2.2. Gas-phase model

Growth of amorphous silicon layers within a PECVD reactor is intimately tied to the physio-chemical phenomena that govern the gas phase. Mass, momentum and energy balances each play a key role in predicting the conditions at the shared boundary between the macroscopic and microscopic domains. To that end, traditional analytic solutions to the gas-phase model are viable only for simplified geometries or systems which fail to provide meaningful results that can be applied to industrially used PECVD systems. By defining the mesh structure as described in the previous section, numerical methods may be introduced which are capable of solving the complex computational fluid dynamics equations with high resolution. Specifically, at every time step, the governing equations are discretized in alignment with the cell distribution presented in Fig. 1b, allowing for the ANSYS Fluent solver to implement finite volume methods. Extended functionality of the Fluent solver (i.e., a tailored solution specific to deposition via PECVD) is achieved using the aforementioned user defined functions (see Fig. 2 for an example tetrahedral cell element as viewed by the solver).

The continuity, energy and momentum equations employed in this work are standard and as such will be presented only briefly without rigorous derivation. An in-depth description of the flow field equations can be found in the Fluent user manual (ANSYS Inc., 2013). In a generalized vector form, the governing equations are given by the following system:

$$\frac{\partial}{\partial t}(\rho \vec{v}) + \nabla(\rho \vec{v}\vec{v}) = -\nabla p + \nabla \bar{\bar{\tau}} + \rho \vec{g} + \vec{F} \qquad (1)$$

$$\bar{\bar{\tau}} = \mu \left[(\nabla \vec{v} + \nabla \vec{v}^T) - \frac{2}{3}\nabla \vec{v}I \right] \qquad (2)$$

$$\frac{\partial}{\partial t}(\rho E) + \nabla(\vec{v}(\rho E + p)) = \nabla(k\nabla T - \Sigma h\vec{J} + (\bar{\bar{\tau}}\vec{v})) + S_h \qquad (3)$$

$$\frac{\partial}{\partial t}(\rho Y_i) + \nabla \cdot (\rho \vec{v}Y_i) = -\nabla \cdot \vec{J_i} + R_i + S_i \qquad (4)$$

$$\vec{J_i} = -\rho D_{i,m}\nabla Y_i - D_{T,i}\frac{\nabla T}{T} \qquad (5)$$

where ρ is the density of the gas, $\vec{v}$ is the physical velocity vector, p is the static pressure, $\bar{\bar{\tau}}$ and I are the stress and unit tensors,

Table 1
Reactions included in the gas-phase model. Note: Rate constants have units of cm^3/s and have been adopted from the collection prepared by Kushner (1988).

Reaction	Mechanism	Rate constant
R^1	$e^- + H_2 \rightarrow 2H$	7.66×10^{12}
R^2	$e^- + SiH_4 \rightarrow SiH_3 + H$	9.57×10^{13}
R^3	$e^- + SiH_4 \rightarrow SiH_3^+ + H$	3.40×10^{12}
R^4	$e^- + SiH_4 \rightarrow SiH_2 + 2H$	1.13×10^{13}
R^5	$e^- + SiH_4 \rightarrow SiH + H_2 + H$	5.62×10^{12}
R^6	$e^- + SiH_4 \rightarrow Si + H_2 + 2H$	6.70×10^{12}
R^7	$e^- + Si_2H_6 \rightarrow SiH_3 + SiH_2 + H$	2.15×10^{13}
R^8	$e^- + Si_2H_6 \rightarrow H_3SiSiH + 2H$	7.41×10^{13}
R^9	$e^- + Si_3H_8 \rightarrow H_3SiSiH + SiH_4$	3.35×10^{14}
R^{10}	$H + SiH_2 \rightarrow SiH_3$	6.68×10^{11}
R^{11}	$H + SiH_2 \rightarrow SiH + H_2$	1.20×10^{13}
R^{12}	$H + SiH_3 \rightarrow SiH_2 + H_2$	1.20×10^{13}
R^{13}	$H + SiH_4 \rightarrow SiH_3 + H_2$	1.38×10^{12}
R^{14}	$H + H_2Si = SiH_2 \rightarrow Si_2H_5$	3.01×10^{12}
R^{15}	$H + Si_2H_6 \rightarrow SiH_4 + SiH_3$	4.03×10^{12}
R^{16}	$H + Si_2H_6 \rightarrow Si_2H_5 + H_2$	7.83×10^{12}
R^{17}	$H + Si_3H_8 \rightarrow Si_2H_5 + SiH_4$	1.19×10^{12}
R^{18}	$H_2 + SiH \rightarrow SiH_3$	1.20×10^{12}
R^{19}	$H_2 + SiH_2 \rightarrow SiH_4$	1.20×10^{11}
R^{20}	$SiH_2 + SiH_4 \rightarrow Si_2H_6$	6.02×10^{12}
R^{21}	$SiH_3 + SiH_3 \rightarrow SiH_4 + SiH_2$	4.22×10^{12}
R^{22}	$SiH_3 + SiH_3 \rightarrow Si_2H_6$	6.02×10^{12}
R^{23}	$SiH + SiH_4 \rightarrow Si_2H_5$	1.51×10^{12}
R^{24}	$SiH_2 + SiH_4 \rightarrow H_3SiSiH + H_2$	6.02×10^{12}
R^{25}	$SiH_2 + Si_2H_6 \rightarrow Si_3H_8$	7.23×10^{13}
R^{26}	$SiH_2 + SiH_3 \rightarrow Si_2H_5$	2.27×10^{11}
R^{27}	$SiH_3 + SiH_3 \rightarrow SiH_4 + SiH_2$	4.06×10^{13}
R^{28}	$SiH_3 + Si_2H_6 \rightarrow SiH_4 + Si_2H_5$	1.98×10^{13}
R^{29}	$Si_2H_5 + SiH_4 \rightarrow SiH_3 + Si_2H_6$	3.01×10^{11}
R^{30}	$SiH_3 + Si_2H_5 \rightarrow Si_3H_8$	9.03×10^{13}
R^{31}	$H_3SiSiH + SiH_4 \rightarrow Si_3H_8$	6.02×10^{12}
R^{32}	$Si_2H_5 + Si_2H_5 \rightarrow Si_3H_8 + SiH_2$	9.03×10^{13}
R^{33}	$H_3SiSiH \rightarrow H_2Si = SiH_2$	2.71×10^{13}
R^{34}	$H_2Si = SiH_2 \rightarrow H_3SiSiH$	2.29×10^{10}

J is the diffusive flux, Y_i is the mass fraction of species i, D_i is the diffusion coefficient of species i, and S_h, R_i and S_i are terms specific to the UDFs utilized in this work and will be defined below.

As mentioned in the previous subsection, three predominant UDFs are used to tailor the functionality of the generalized Fluent solver to the problem of interest in this work, the first of which accounts for the volumetric reactions occurring above the substrate surface. Although extensive reaction sets have been proposed which detail all possible intermediate and aggregate species involved in the deposition of a-Si:H films (e.g., Kushner (1988)), here we limit the scope to the twelve most dominant species and their associated thirty-four gas-phase reactions. A complete listing of the reactions, mechanisms and rate constants are given in Table 1. Thus, the R_i terms in the mass balance presented above are a product of this reaction set and are updated by the UDF during each time step.

The terms S_h and S_i appearing in Eqs. 3 and 4, respectively, refer to user defined sources or sinks. During the deposition of amorphous silicon, mass is drawn from the gas phase in the form of SiH$_3$ and H radicals, and mass is likewise reintroduced to the macroscopic domain due to hydrogen abstraction from the substrate surface via the formation of the stable species, SiH$_4$ (note: this phenomena is visible in Fig. 4a). The S_i term acts as a dynamic boundary condition which is updated based on the transfer of mass during the previous microscopic simulation cycle, with units of kg s^{-1}m^{-2}. In other words, at the end of a time step the amount of mass (for each species) withdrawn from, or introduced to, the macroscopic domain is reported from the individual microscopic calculations. Subsequently, the boundary conditions for the two-dimensional areas which define the interfaces of the kMC regions are updated before the next time step commences. Additionally, the formation and breaking of chemical bonds along the
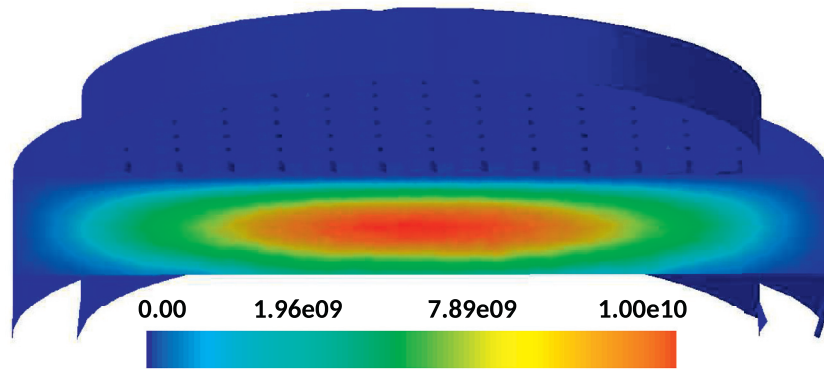
Fig. 3. Electron density within 3D axisymmetric PECVD geometry (cm^{-3}).

(a) 3D boundary cell

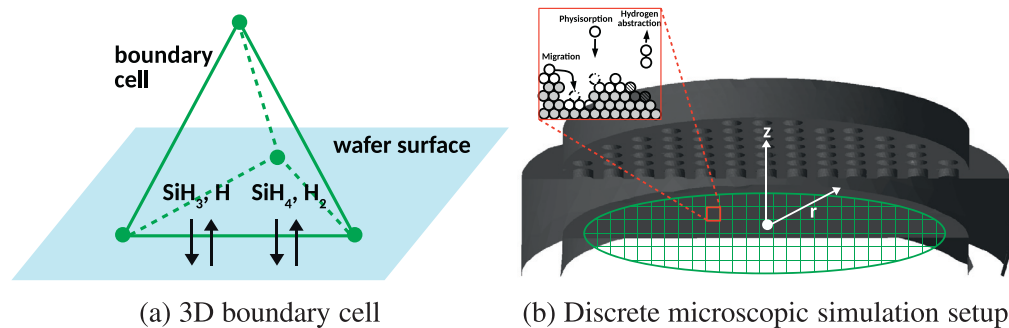(b) Discrete microscopic simulation setup

Fig. 4. (a) Finite element adjacent to the substrate surface with dynamic boundary condition calculated via microscopic simulation domain. (b) Kinetic Monte Carlo setup within overall multiscale simulation. Wafer substrate discretized in both the *x* and *y* directions forming a 'grid' structure.

amorphous surface causes an exchange of energy between the substrate and the continuous gas phase which is tracked through the S_h term. For clarification on the dynamic boundary conditions and their role in the overall multiscale model, please refer to the multiscale workflow section below.

2.2.1. Electron density profile

In looking at Table 1, reactions R^1 through R^9 involve the interaction of free electrons and stable species; these nine reactions define the plasma chemistry necessary for the deposition of SiH$_3$ and H. As such, the electron density is key to the accuracy of the plasma phase and the corresponding growth of thin film layers. For plasmas generated from radio frequency (RF) discharges within cylindrical geometries, literature has shown that the electron density can be accurately estimated from the product of the zero order Bessel function and a sine function whose period is twice the distance between the showerhead and wafer substrate (Park and Economou, 1991). This is described by the following equation:

$$n_e(r, z) = n_{eo} \cdot J_0\left(2.405\frac{r}{r_t}\right) \cdot \sin\left(\frac{\pi z}{D}\right), \qquad (6)$$

where n_{eo} is the maximum electron density, J_0 is the zero order Bessel function of the first kind, r_t is the radius of the reactor, and D is the distance between the showerhead and wafer (i.e., the parallel plate spacing). The distribution seen in Fig. 3 is the result of applying the aforementioned electron density to the three-dimensional PECVD geometry presented earlier. The free electron 'cloud' remains bounded by the charged region between the cylindrical walls of the reaction chamber and the parallel plates which make up the showerhead and substrate platform. As expected, the zero order Bessel function enforces a maximum density in the center of the reactor which trails off near the exit ports along the edge.

2.3. Microscopic domain

While the CFD model itself, along with the UDFs for the gas phase reactions and electron density, define the macroscopic domain, the microscopic domain is contained entirely within the third and final UDF; specifically, as radicals diffuse from the gas phase down to the substrate surface, they enter the microscopic domain. In looking at Fig. 4a, finite elements (i.e., mesh cells) which share a boundary with the substrate surface allow for the exchange of SiH$_3$ and H radicals. This mechanism makes possible the interconnection between the two distinct simulation domains. While tracking of each individual particle remains a computationally infeasible task, growth of *a*-Si:H thin film layers may still be achieved using a network of parallel kinetic Monte Carlo (kMC) algorithms. Specifically, the substrate surface is broken down into discrete regions along the $x - y$ plane as shown in Fig. 4b, and within each region an independent kMC simulation is executed. Each simulation consists of a lattice of width 1200 particles which captures the growth of a representative *a*-Si:H layer within the associated region. The tetrahedral cells bordering each region are assigned dynamic boundary conditions corresponding to the exchange of mass and energy due to thin film growth at each time step (see Fig. 4a). Details concerning the development of the microscopic UDF, including both the parallel kMC structure and dynamic boundary conditions, will be discussed in detail in the following subsections.
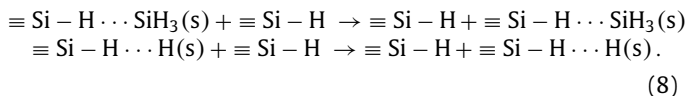
2.3.1. Thin-film growth chemistry

Before the microscopic model is presented, it is important to detail the chemical phenomena which occur along the surface of the growing thin film layer. Only SiH_3 and H appear in this text as deposition species due to experimental results from Perrin et al. (1998) and Robertson (2000) which indicate that greater than 98% of amorphous silicon deposition can be attributed to these species alone.

In order for growth of the *a*-Si:H thin film to occur, particles must diffuse from the gas phase to the wafer substrate, and subsequently stick to the hydrogenated surface. Upon striking the surface, SiH_3 and H radicals may either be deflected back into the gas phase or physisorption may occur at hydrogenated silicon sites ($\equiv Si - H$) as evidenced by the following reaction set:

$$SiH_3(g) + \equiv Si - H \rightarrow \equiv Si - H \cdots SiH_3(s)$$
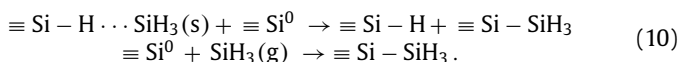$$H(g) + \equiv Si - H \rightarrow \equiv Si - H \cdots H(s). \tag{7}$$
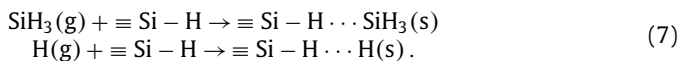
The probability for a particle which strikes the surface to remain on the surface is known as the sticking coefficient and will be considered in the kinetic Monte Carlo section to follow. Once a weak hydrogen bond has been formed, physisorbed radicals may follow one of two distinct mechanisms; the first and most dominant of which is rapid diffusion across the surface of the lattice via migration:

$$\equiv Si - H \cdots SiH_3(s) + \equiv Si - H \rightarrow \equiv Si - H + \equiv Si - H \cdots SiH_3(s)$$
$$\equiv Si - H \cdots H(s) + \equiv Si - H \rightarrow \equiv Si - H + \equiv Si - H \cdots H(s). \tag{8}$$

Alternatively, a particle may return to the gas phase through the abstraction of a surface hydrogen,

$$\equiv Si - H \cdots SiH_3(s) + \equiv Si - H \rightarrow \equiv Si - H + \equiv Si^0 + SiH_4(g), \tag{9}$$
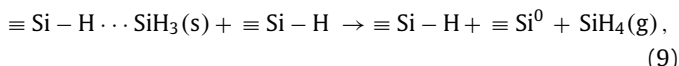
whereby a physisorbed radical removes a neighboring hydrogen atom and reforms the stable species (e.g., SiH_4 or H_2 in the case of two species deposition). This process leaves behind dangling bonds ($\equiv Si^0$) which are crucial to the growth of the amorphous silicon film. Growth of the lattice proceeds unit by unit via chemisorption of SiH_3 at dangling bond sites (i.e., the Si atom forms a covalent bond, permanently fixing its location within the amorphous structure) as shown in the following reactions:

$$\equiv Si - H \cdots SiH_3(s) + \equiv Si^0 \rightarrow \equiv Si - H + \equiv Si - SiH_3$$
$$\equiv Si^0 + SiH_3(g) \rightarrow \equiv Si - SiH_3. \tag{10}$$

The second reaction listed above suggests a gas phase radical may directly chemisorb at an existing dangling bond site without first migrating around the hydrogenated surface. While these events are unlikely due to the relative infrequency of dangling bonds across the surface area of the *a*-Si:H film, they are not strictly forbidden and must be considered in the development of the microscopic model. It is important to note that chemisorption of H only results in a return of the surface to its original, hydrogenated state:

$$\equiv Si - H \cdots H(s) + \equiv Si^0 \rightarrow \equiv Si - H + \equiv Si - H$$
$$\equiv Si^0 + H(g) \rightarrow \equiv Si - H. \tag{11}$$
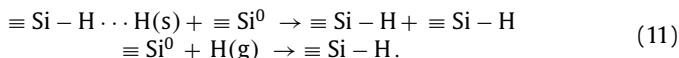
A simplified illustration of the surface chemistry can be seen in Fig. 5.

2.3.2. Lattice characterization and relative rates

In our early work on modeling PECVD systems (Crose et al., 2015), a solid-on-solid (SOS) lattice was used to represent the microscopic structure of the growing *a*-Si:H thin film. Although a two-dimensional SOS lattice remains the most efficient lattice structure from a computational standpoint, no vacancies or voids are permitted within the bulk material. Given that experimentally grown *a*-Si:H layers are observed to have void fractions in

the range of 10–20%, our recent works have alternatively utilized a triangular framework (Crose et al., 2017a,b). By eliminating the restriction of SOS behavior and introducing close-packed groups with a minimum of two nearest neighbors, overhangs may develop which in turn lead to voids in the triangular lattice (see Fig. 6). It is important to note that while the overall multiscale model operates in three dimensional space, the lattice which defines the microscopic domain remains two dimensional. Although the effort required to expand the lattice structure into a third coordinate is relatively minimal, the computational cost of doing so would be non-trivial. Given that the goal of the microscopic model (i.e., the lattice structure and associated kinetic Monte Carlo algorithm), is to capture the growth rate of amorphous silicon deposition, nothing would be gained from a three dimensional lattice; particle interactions, void formation and steric hindrance are accurately expressed in the proposed triangular lattice model.

Each grid location defined in Fig. 7 represents an independent microscopic simulation. Within these discrete grid cells exists a representative triangular lattice whose size can be characterized by the product of the length and thickness. The number of lateral sites is denoted by L and is proportional to the physical lattice length by $0.25 \times L$, given a hard-sphere silicon diameter of ~ 0.25 nm. The thickness, τ, may be calculated from the number of monolayers, H, by the following equation:

$$\tau = 0.25 \cdot H \cdot \frac{\sqrt{3}}{2}, \tag{12}$$

where the factor 0.25 accounts for the diameter of individual silicon atoms and $\sqrt{3}/2$ accounts for the reduction in thickness due to the offset monolayers which result from the close-packed structure of the triangular lattice (refer to Fig. 6). The number of lateral sites remains fixed at $L = 1200$ for each discrete microscopic simulation zone. This length allows for adequate development of thin film morphology and reduces wall effects without being so large as to necessitate the inclusion of spatial variations across individual lattices. To be clear, while significant gradients exist in the species concentrations within the PECVD reactor and from one grid location to another (e.g., Figs. 4b and 7), finite microscopic simulations of length ~ 300 nm can be assumed to experience uniform deposition.

Migration and hydrogen abstraction involve species which exist on the surface of the thin film; as a result, these reactions are thermally activated events and follow a standard Arrhenius-type formulation:

$$r_{t,i} = \nu_i e^{-E_i/k_B T}, \tag{13}$$

where ν_i is the attempt frequency prefactor (s^{-1}) and E_i is the activation energy of radical i. Frequency prefactor and activation energy values are drawn from Bakos et al. (2005, 2006) to correspond to the growth of *a*-Si:H films via the two species deposition of SiH_3 and H.

Physisorption events originate within the gas-phase and can be described by an athermal or barrierless reaction model based on the fundamental kinetic theory of gases which yields the following rate equation:

$$r_{a,i} = J_i s_c N_a \sigma, \tag{14}$$

where J is the flux of gas-phase radicals, s_c is the local sticking coefficient (i.e., the probability that a particle which strikes the surface will 'stick' rather than bouncing off), N_a is the Avogadro number, and σ is the average area per surface site. Eqs. (15)–(17) can be used to calculate the flux, J:

$$J_i = \eta_i \bar{u}_i, \tag{15}$$
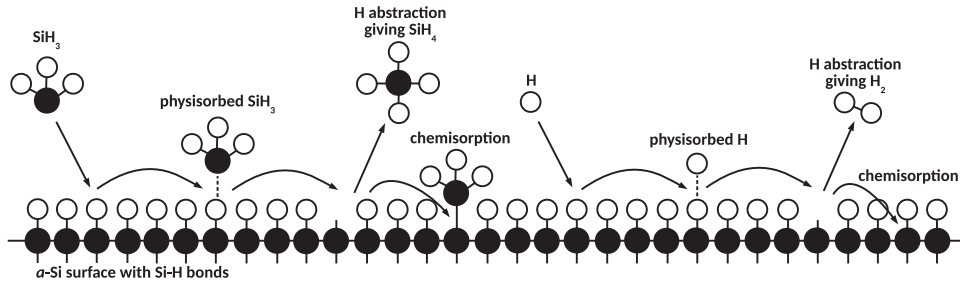
$$\eta_i = \frac{p_i}{RT}, \tag{16}$$

Fig. 5. Chemical model illustration showing particle-surface interactions.
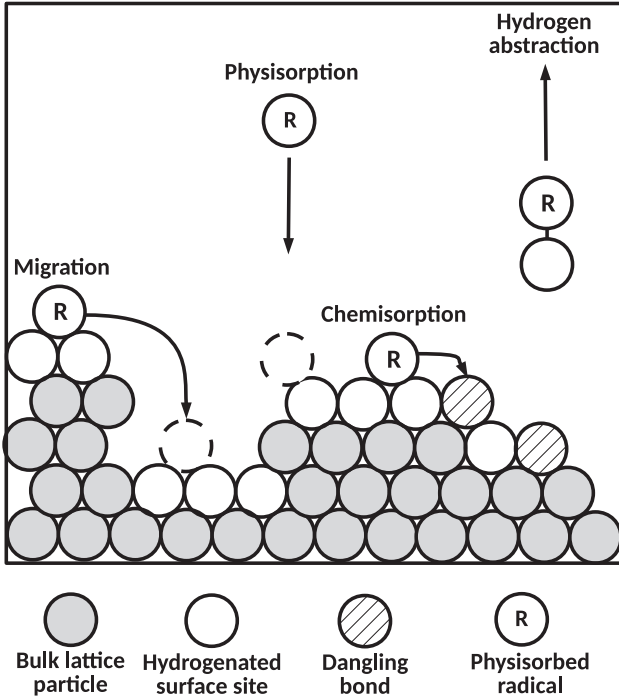

Fig. 6. Triangular lattice representation showing four microscopic processes. Processes from left to right: migration, physisorption, chemisorption, and hydrogen abstraction.
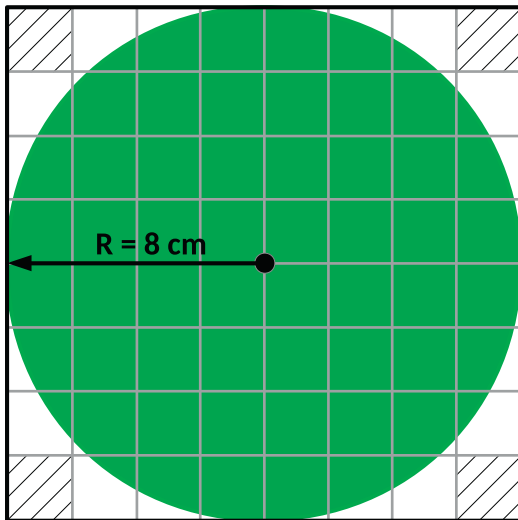

Fig. 7. Spatial distribution of kinetic Monte Carlo simulations. One representative microscopic simulation (i.e., a 1200 particle wide lattice) is executed within each overlapping grid location. The hashed corners represent regions which do not overlap the substrate surface.

$$\bar{u}_i = \sqrt{\frac{8k_B T}{\pi m_i}}, \qquad (17)$$

where η_i is the number density of radical i (here the reactive gas-phase is assumed to be ideal), $\bar{u}_i$ is the mean radical velocity, p_i is the partial pressure of i, R the gas constant, T is the temperature, k_B is the Boltzmann constant, and m_i is the molecular weight of radical i. By substitution of the expression for J into Eq. (14), the overall reaction rate for an athermal radical i becomes:

$$r_{a,i} = \frac{p_i}{RT} \sqrt{\frac{8k_B T}{\pi m_i}} s_c N_a \sigma. \qquad (18)$$

The relative magnitude of these reaction rates determines their frequency within the microscopic simulation, as will be discussed at length in the following subsection.

2.3.3. Kinetic Monte Carlo algorithm

The aforementioned lattice structure defines the scope and interaction of particles within the microscopic domain; however, the evolution of the lattice microstructure (i.e., growth of thin film layers on the wafer substrate) is achieved using a hybrid n-fold kinetic Monte Carlo algorithm for which the overall reaction rate is defined by

$$r_{\text{total}} = r_a^{SiH_3} + r_a^{H} + r_t^{abs}, \qquad (19)$$

where $r_a^{SiH_3}$ is the rate of physisorption of SiH$_3$, r_a^{H} is the rate of physisorption of H, and r_t^{abs} is the rate of hydrogen abstraction forming SiH$_4$ (note: the subscripts a and t denote athermal and thermally activated reactions, respectively). In the interest of computational efficiency, surface migration is decoupled and does not contribute to the overall rate. Specific details regarding the motivation for decoupling migration events and the associated procedure for doing so are provided at the end of this section.

Each kMC cycle begins through generating a uniform random number, $\gamma_1 \in [0, 1]$. If $\gamma_1 \leq r_a^{SiH_3}/r_{\text{total}}$, then an SiH$_3$ physisorption event is executed. If $r_a^{SiH_3}/r_{\text{total}} < \gamma_1 \leq (r_a^{SiH_3} + r_a^{H})/r_{\text{total}}$, then a hydrogen radical is physisorbed. Lastly, if $\gamma_1 > (r_a^{H} + r_t^{abs})/r_{\text{total}}$, then a surface hydrogen is abstracted via SiH$_3$.

Execution of physisorption events, regardless of radical type, proceed through selecting a random site on the surface of the triangular lattice from a list of candidate sites. Acceptable candidate sites consist of those which exist in their standard, hydrogenated state, or which contain a dangling bond left behind from a hydrogen abstraction event; sites which currently host a physisorbed radical cannot accept additional physisorption events. If the chosen site contains a dangling bond, the particle is instantaneously chemisorbed, and in the case of SiH$_3$ radicals the lattice to grows by one. Hydrogen abstraction occurs by selecting a random SiH$_3$ particle from the surface of the lattice and returning it to the gas-phase as the stable species, SiH$_4$. In other words, a migrating SiH$_3$
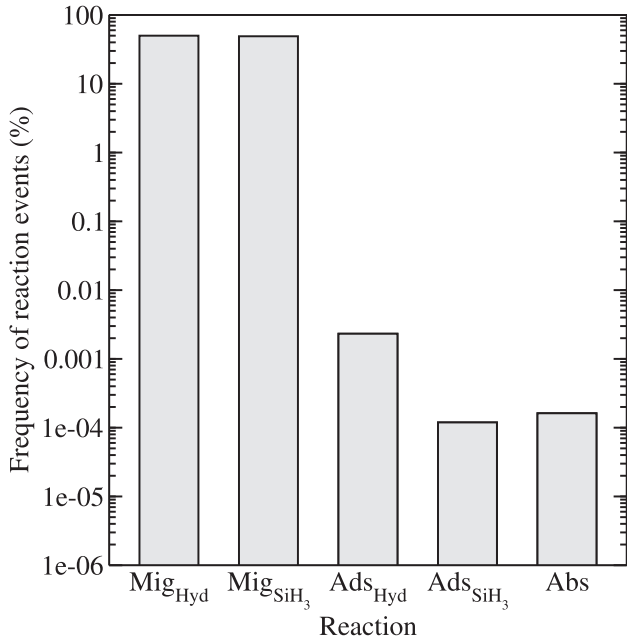
Fig. 8. Normalized frequency of reaction events within the present kMC scheme at $T = 475$ K, $P = 1$ Torr, and a SiH_4^{in} mole fraction of 0.9.

radical removes a hydrogen atom from the surface of the film leaving behind a dangling bond in its place. Although physisorbed hydrogen radicals may also abstract a hydrogen atom to reform the diatomic species, the high activation energy required causes these events to be infrequent at the deposition conditions of interest. A second random number, γ_2 is now sampled in order to calculate the time required for the completed kMC event:

$$\delta t = \frac{-\ln(\gamma_2)}{r_{\text{total}}}, \qquad (20)$$

where $\gamma_2 \in (0, 1]$ is a uniform random number.

Up to this point, migration has been excluded from the discussion of kMC events. In looking at Fig. 8, it is clear that migration is the dominant interaction mechanism within the growing lattice structure. Brute force kMC methods (in which all event types are available for execution) require more than 99% of computational resources to be spent on migration alone (note: the results in Fig. 8 are typical for a-Si:H systems operating near $T = 475$ K and $P = 1$ Torr). Consequently, only a small fraction of simulation time contributes to events leading directly to film growth while the vast majority is spent on updating the locations of rapidly moving particles. In a continual effort to reduce the computational demands of the overall multiscale model, any savings that result from the microscopic domain are of great interest. To that end, a Markovian random-walk process has been introduced which successfully decouples particle migration from classic kMC algorithms.

Traditionally, a kMC cycle is defined by the execution of single event which moves forward the physical time of the system. The hybrid kinetic Monte Carlo scheme presented here requires two successive steps per cycle: first, a kMC event is executed according to the relative rates of $r_a^{SiH_3}$, r_a^H and r_t^{abs} as presented above; second, a propagator is introduced to capture the motion of physisorbed radicals. The total number of propagation steps is $N_H + N_{SiH_3}$ where

$$N_H = \frac{r_t^H}{r_a^H + r_t^{abs} + r_a^{SiH_3}}, \quad N_{SiH_3} = \frac{r_t^{SiH_3}}{r_a^H + r_t^{abs} + r_a^{SiH_3}}, \qquad (21)$$

and r_t^H and $r_t^{SiH_3}$ are the thermally activated migration rates of hydrogen and silane radicals, respectively. In other words, the total

number of random walk steps is in proportion to the magnitude of the migration rates, and each set of propagation steps, N_H and N_{SiH_3}, are split evenly among the current number of physisorbed radicals, n_H and n_{SiH_3}. The radicals then initiate a series of two-dimensional random walk processes according to the number of assigned propagation steps. Thus, the bulk motion of the propagator approximates the intricate movements of a given particle. In the interest of clarity, the procedure for the random walk process is as follows: a radical species is chosen, a random physisorbed radical of the given species is selected, the weighted random walk consisting of N_i/n_i propagation steps begins, propagation continues until either N_i/n_i steps have been executed or the movement terminates prematurely when a radical becomes chemisorbed at a dangling bond site, the final position of the propagator is then stored as the radical's new position and this cycle continues until all $n_H + n_{SiH_3}$ physisorbed species have migrated. The weighting of each propagation step is designed such that the probability for a particle to relax down the lattice is exponentially higher than 'jumping' up lattice positions (i.e., migration down the lattice is favored), and likewise, the probability of 'jumping' to nearby locations is higher than distant ones. The net result of this method is relaxation and particle tracking are only required to be updated once per particle rather than after each individual particle movement, as in brute force methods. The time required for an individual migration step is calculated in much the same way as physisorption or hydrogen abstraction:

$$\delta t_H = \frac{-\ln(\gamma_i)}{r_t^H}, \quad \delta t_{SiH_3} = \frac{-\ln(\gamma_j)}{r_t^{SiH_3}}. \qquad (22)$$

Thus, the total time elapsed for all migration events, Δt, is determined by summation over the number of propagation steps per radical type,

$$\Delta t = \sum_i^{N_H} \frac{-\ln(\gamma_i)}{r_t^H} + \sum_j^{N_{SiH_3}} \frac{-\ln(\gamma_j)}{r_t^{SiH_3}}. \qquad (23)$$

In this manner, the elapsed time for the microscopic domain moves forward towards the completion of the time step set by the macroscopic, CFD solver.

Although our methodology of decoupling the diffusive processes from the remaining kinetic events represents significant computational savings, we must validate that doing so does not alter the overall morphology or characteristics of the resulting a-Si:H thin film. Validation of the Markovian random walk approximation is achieved via two mechanisms: (1) ensuring that surface morphologies and film porosities observed are appropriate for the chosen process parameters, and (2) that growth rates remain on par with experimental values. Detailed model validation can be found in the earlier works of Crose et al. (2017b). It is important to note that film growth continues in this cyclic manner until the kMC algorithm has reached the alloted time step (i.e., until the microscopic model has caught up with the macroscopic, CFD solver). For a more in-depth discussion of the transient operation of the multiscale model, please refer to the following section.

2.4. Multiscale workflow

The methodology for connecting the macro- and microscopic domains is of particular importance to the function of the multiscale model; consequently, the simulation workflow must be examined here. In Fig. 9, the top and bottom regions denote execution of macroscopic and microscopic events, respectively. At the start of each transient batch simulation, $t = 0$, every cell of the mesh will first solve the governing equations with respect to their reduced spatial coordinates using finite volume methods, then the boundaries along adjacent cells are resolved iteratively. In order to
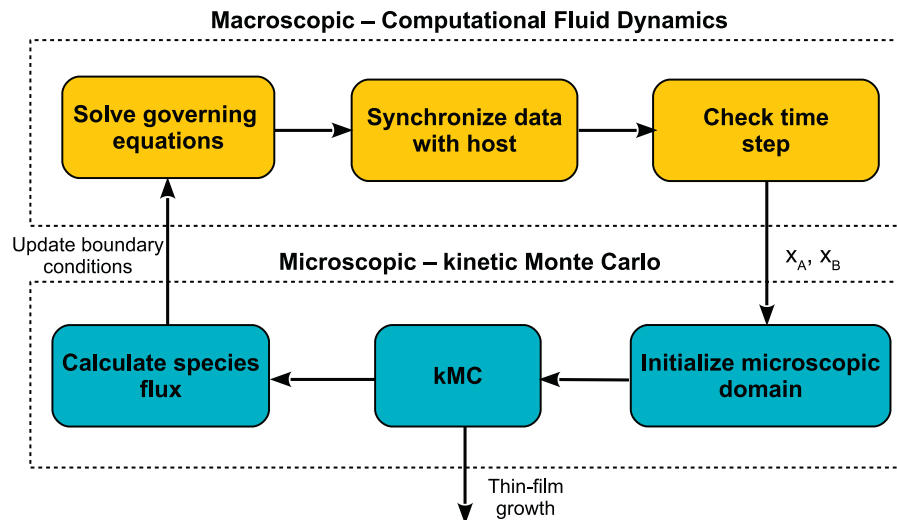
Macroscopic – Computational Fluid Dynamics

Fig. 9. Multiscale simulation workflow detailing the coordination between the macroscopic and microscopic events.

move forward in time, an Implicit Euler scheme is utilized (note: a detailed methodology is available in the Fluent user manual, ANSYS Inc. (2013)). Additionally, the first two UDFs (e.g., the volumetric reaction and electron density scripts) are executed and the results of which are fed into Fluent's PDEs. Once a time step has been completed, $t = t_1$, the species concentration, the temperature and the pressure along the boundary of the wafer substrate are transferred to the microscopic domain (e.g., Fig. 4a and and the right-hand side of Fig. 9). The discrete kMC simulations discussed in the previous section are then initialized using this information allowing for growth of a-Si:H thin film layers to begin. Once all of the microscopic simulations have reached t_1, the dynamic boundary conditions for cells bordering the wafer surface are updated based on the mass and energy transfer within the associated region (e.g., Figs. 4 and 9, left). Again, the macroscopic PDEs are solved such that the time moves forward to t_2 and the cycle continues. In this way, the multiscale model progresses until the end of the batch deposition process is reached (i.e., until $t = t_{batch}$).

Given that the kinetic Monte Carlo algorithm is unable to span the entire substrate surface in a single microscopic simulation (refer to Figs. 4b and 7), it is necessary to interpolate between known data points when updating the boundary conditions. Specifically, boundary cells which lie between kMC simulation locations are assigned mass and energy transfer values based on interpolation between the three nearest data points. In other words, every set of three nearest data points forms a triangular surface which provides boundary condition data for all mesh cells contained within that region. Further details concerning the execution of the discrete kMC simulations will be provided in the following section. As a final note, it is important to clarify the relative differences in the time constants for each domain. The gas-phase reactions reach equilibrium within the first few seconds of reactor operation. Conversely, while the individual surface interactions on the silicon thin film are rapid, growth of the thin film layer is continuous throughout the batch cycle. As a result, for the specific reactor geometry and reaction set used in this work it would be feasible to switch off calculations of the macroscopic domain after the initial transience dies out. This would improve the computational speed of the model in some cases at the cost of generality and with a loss in accuracy at the boundary between the two domains. More importantly, applicability of the model to other reactor designs, multiscale systems and deposition methods would be lost (e.g., atomic layer deposition studies).

2.5. Parallel computation

The move from 2D to 3D PECVD reactor models comes at the cost of computational efficiency. In the recent work of Crose et al. (2017b), the 2D axisymmetric CFD simulations required the use of a message passing interface (MPI) structure in order to parallelize the domain and to achieve feasible computation times (e.g., < 1 day per batch simulation), as is common practice in systems with non-trivial computational requirements (Ingle and Mountziaris, 1995; Kwon, JSI. et al., 2015). In this work, the computational demands are further increased due to the mesh containing ∼ 1.5 million cells (as opposed to 120,000 for the 2D model), tetrahedral cell shape and far more discrete kMC simulations required to span the substrate surface. It is important to keep in mind that the results presented in the following sections represent not only the culmination of several test batches necessary to the development of the multiscale model, but also data that has been averaged across several redundant simulations; therefore, serial computation on a single processor or workstation corresponds to an infeasible task. As a result, the parallel computation strategy detailed here remains crucial to operation of transient simulations in order to mitigate the aforementioned computational demands.

In addition to the primary motivation of reducing simulation time, two other key benefits motivate the extra effort necessary in utilizing parallel programming. First, kMC simulations inherently exhibit noise due to the stochastic nature of event selection and particle movement. By maintaining constant deposition parameters and repeating simulations numerous times, we can reduce the noise level and obtain more accurate, averaged values. Second, it is often useful to perform many simulations at different conditions (e.g., when searching for suitable model parameters) without having to schedule several serial batch runs.

The details of the parallel algorithm itself, as well as the associated message-passing interface (MPI) structure, are standard and therefore will not be expanded upon at this time. In-depth studies of parallel processing with applications to microscopic simulations have been made by Cheimarios et al. (2016); Nakano et al. (2001), and the recent work of Kwon, JSI. et al. (2015) provides the basis on which this work is built upon. That being said, a brief outline of parallel programming structure and its application to this work is useful in clarifying the simulation workflow and will be provided below.

The process for creating a parallel program can be understood through three elementary steps: (1) the original serial task is de-
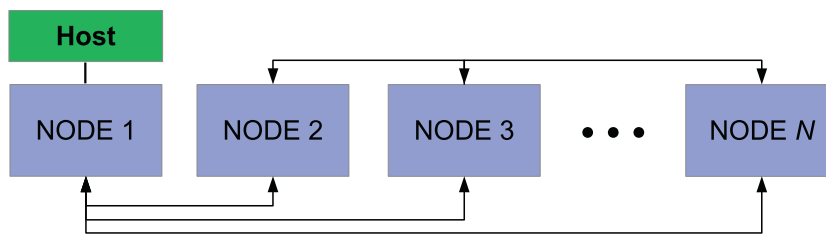
Fig. 10. Communication between host and nodes within the MPI architecture.

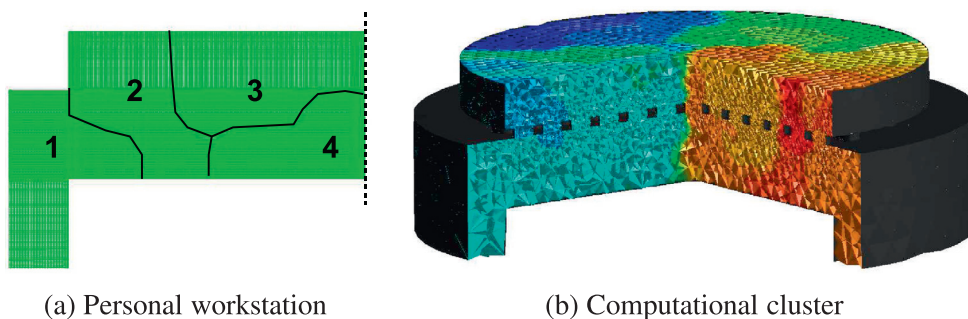(a) Personal workstation   (b) Computational cluster

Fig. 11. (a) Distribution of 2D structured mesh across computational cores on a typical personal workstation with a quad-core CPU. (b) Unstructured mesh containing 1.5 million cells distributed across 128 computational cores (note: the colored regions denote different assignments).

composed into small computational elements; (2) tasks are distributed across multiple processors; and (3) a host node orchestrates communication between processors at the completion of each time step. As shown in Fig. 10, nodes 2 through N pass information to node 1 which in turn forwards information to the host node. The number of available nodes is dependent on the architecture of the workstation or computational cluster used, and often a node on a computational cluster may contain multiple computing cores. In an effort to generalize the discussion, nodes and cores will be used interchangeably throughout this work, as would be the case on a cluster with one core per node. Fig. 11a provides an example for distributing the cells of a 2D mesh across 4 cores of a personal workstation; similarly, Fig. 11b shows the distribution of mesh elements across 64 cores as used in this work. The maximum achievable speedup given the aforementioned parallel programming strategy can be defined by:

$$M(N) = \frac{1}{(1+P) + \frac{P}{N}}, \tag{24}$$

where M is the maximum achievable speedup, P is the fraction of the program which is available for parallelization (i.e., the fraction of the original task which may be discretized), and N is the number of processors utilized (Culler et al., 1999).

In reality, the maximum speedup (i.e., execution speed multiplier) deviates from this formulation for two reasons. First, as the number of cores increases, so does the overhead time for communication between cores and the host node. Second, only the serial computations defining the macroscopic (CFD) domain may be strictly decomposed into smaller tasks. As discussed, the PECVD reactor mesh can be distributed across the 64 cores utilized in this work; however, the microscopic kMC simulations are unable to be decomposed. Given the relatively small lattice size (1200 nm) as compared to the overall dimension of the reactor, decomposition of a single lattice would provide little benefit while introducing significant computational overhead necessary for resolving the shared lattice boundaries. Instead, we can exploit the fact that the kMC simulations across the substrate surface are independent of one another and may be distributed among the available nodes. In other words, while a single kMC simulation should not be decomposed, the many independent kMC simulations necessary for span-
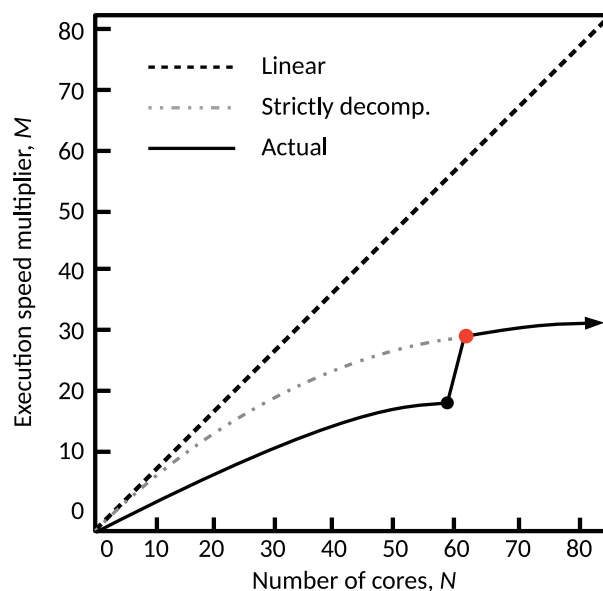

Fig. 12. Expected speed-up due to parallelization across N nodes.

ning the substrate surface can be distributed to speedup the overall multiscale simulation. The resulting speedup due to the combination of these methods can be seen in Fig. 12. The linear 1:1 speedup is never achievable due to the communication overhead but provides a benchmark for comparison. The continuous grey curve represents the theoretical speedup if the multiscale simulation was strictly decomposable. Finally, the actual multiplier curve exhibits a sharp jump between 59 and 60 cores. Given that the parallel simulations used in this work are synchronized (i.e., faster nodes must wait for slower nodes to complete a time step before execution continues), if even one node is forced to run two microscopic kMC simulations, the remaining $N-1$ nodes must sit idle. Since 60 kMC locations are used to span the substrate surface (see the microscopic modeling section), the number of nodes, N, is recommended to be greater than 60.
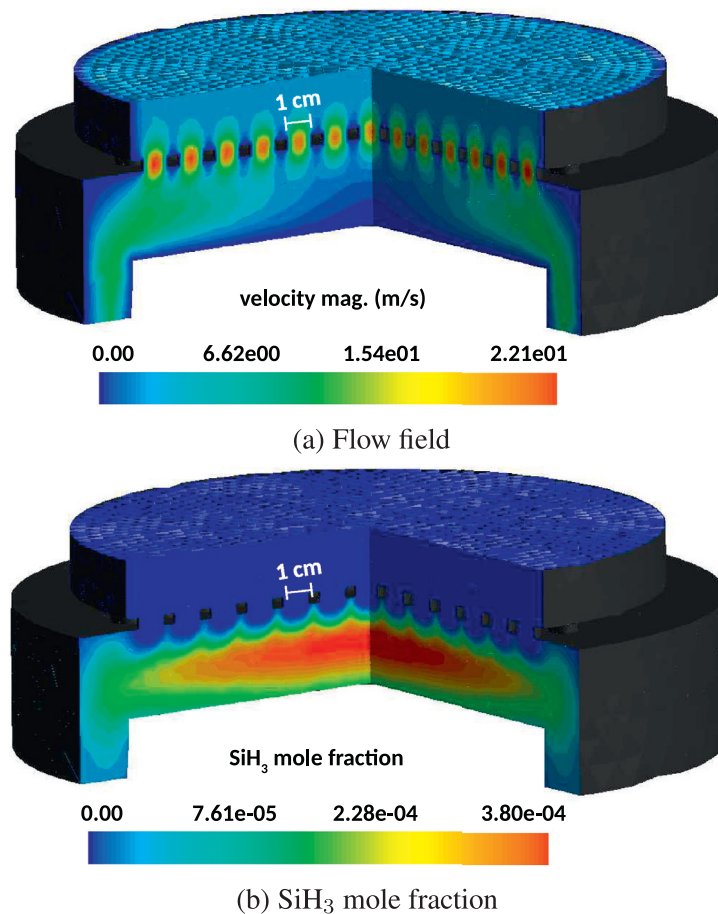
(a) Flow field

(b) SiH$_3$ mole fraction

Fig. 13. (a) Velocity magnitude within 3D PECVD reactor showing dead-zone near substrate center. (b) Non-uniform, steady-state SiH$_3$ concentration.

3. Results

The results presented in the following subsections represent the long-time behavior of the PECVD reactor at operating conditions of $T = 475$ K, $P = 1$ Torr and an inlet gas flow rate of 75 SCCM at a 10:1 ratio of hydrogen to silane. Although the simulations presented in this work are entirely transient in nature, the startup period of the reactor is relatively brief and therefore will not be discussed at this time. Instead, the three dimensional contour maps shown below have been drawn from $t = 320$ s, roughly half way through the thin film growth period after the transient dynamics in the gas phase have largely died out. Note, the reactor never reaches a steady-state due to the continual particle interactions and growth within the microscopic domain. Given that the deposition of a-Si:H layers via PECVD is a batch process, the thickness measurements reported have been drawn at the completion of a batch, $t_{batch} = 640$ s, the time required to complete deposition of a 300 nm thick film. Additionally, thickness measurements have been averaged across 10 redundant batch simulations to minimize stochastic effects due to the kinetic Monte Carlo model.

3.1. Non-uniform deposition

Fig. 13a shows the resulting velocity profile of the gas phase species in the PECVD reactor after the brief startup period. According to the flow field, the gas phase reaches maximal velocity when flowing through the showerhead. Below the showerhead level, the flow velocity is increased near the narrow outlet regions, while at the center the gas flow stagnates in an apparent 'dead zone.' The

velocity distribution suggests that a change of shape or frequency of showerhead holes might influence the flow profile and resulting species distribution. The relationship between flow field and distribution of deposition species is more evident through a direct comparison between Fig. 13a and 13b. Fig. 13b shows that the concentration of SiH$_3$, the deposition species responsible for thin film growth, reaches its maximum at the center of the reactor and diminishes in the radial direction. This is consistent with the flow velocity profile in Fig. 13a as species in regions with a lower flow rate will experience higher residence times (i.e., more time to react and produce silane radicals). This effect is magnified by the electron density profile which defines a maximum electron density, n_{eo} at the center of the cylindrical reaction chamber. In addition, variation in the concentration of SiH$_3$ along the azimuthal, θ, direction is observed. Fig. 14a shows that for a fixed radial position and height, the concentration of SiH$_3$ is non-uniform. A quantitative report of the azimuthal variation in x_{SiH_3} is given in Fig. 15, where the triangular data points represent the SiH$_3$ concentration profile which results from the original showerhead design (i.e., the showerhead design shown in Figs. 13 and 14a).

Due to the interconnection between the macroscopic reactor scale and microscopic thin film domain, it is expected that variations in the deposition species concentration, in particular variations near the substrate surface, will result in thin film products with non-uniform thickness. This effect has been well characterized and is known to cause device quality issues and poor solar conversion in the case of photo-voltaic cells Crose et al. (2017a,b); da Silva and Morimoto (2002). As shown by the upward triangles in Fig. 15b, for the PECVD system described in this work, the mul-
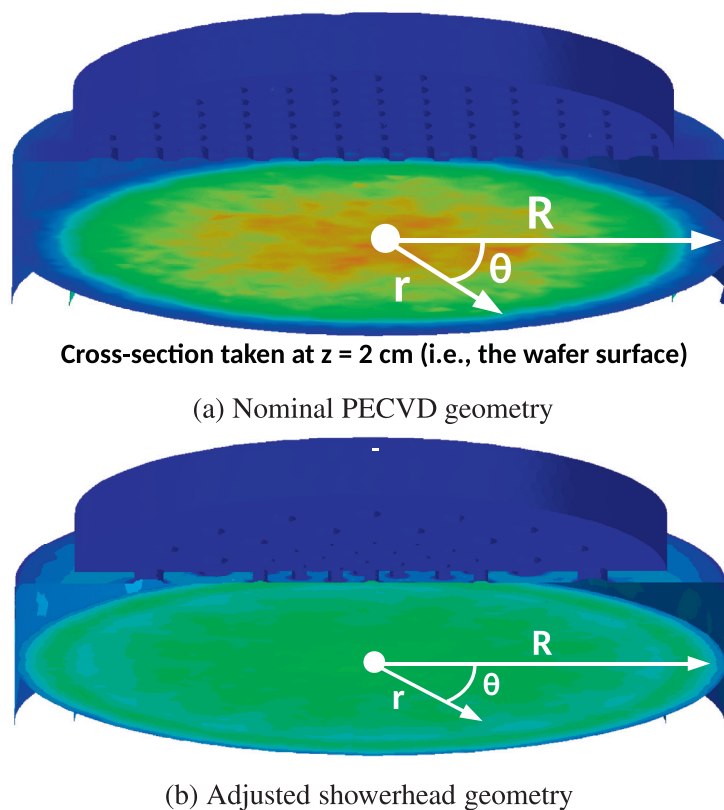
Cross-section taken at z = 2 cm (i.e., the wafer surface)

(a) Nominal PECVD geometry

(b) Adjusted showerhead geometry

Fig. 14. (a) Cross section of SiH_3 concentration taken just above the surface of the wafer substrate (b) SiH_3 concentration above the wafer surface for the adjusted reactor geometry. (For interpretation of the references to color in this figure, the reader is referred to the web version of this article.)

tiscale model suggests that variations in the concentration of SiH_3 and H lead to a thickness offset of 25 nm from the desired set-point of 300 nm near the edge of the wafer substrate. Between $r = 0$ and 4 cm, the thickness offset is relatively minor, within 5 nm of the set-point.

3.2. Adjusted reactor geometry

Compared with simplified 2D multiscale models, the 3D multiscale CFD model presented in this work is able to capture detailed showerhead geometries, and is therefore capable of evaluating alternative PECVD reactor designs. As mentioned in the motivations for this work, improvement to the thickness uniformity of amorphous silicon thin films is of significant interest from a manufacturing perspective. To this end, a modified showerhead design that reduces the spatial non-uniformity of deposition species is proposed here. The original showerhead geometry consists of circular holes with equal diameter, which are distributed in a rectangular array (e.g., Fig. 14a). In the new showerhead design, showerhead holes are arranged in a polar array, and the diameter of the showerhead holes increases in the radial direction from 0.5 to 1 cm, as shown in Fig. 14b.

Computational constraints limit the number of incremental design changes which may be evaluated. Consequently, the proposed showerhead design cannot be claimed to be optimal; instead, adjustments have been made based on the observed results in the previous section. Specifically, larger showerhead hole area near the edge of the reactor allows for more gas flow above the rim of the substrate, which helps diminish the radial variation of SiH_3 concentration. The overall showerhead hole area has

been reduced causing the reactant gases to pass more quickly through the holes and over the substrate surface. Although this change is expected to lead to slower growth of the thin film product, the thickness uniformity should nonetheless improve. In addition, the polar array of showerhead holes is symmetrical with respect to any θ direction, and therefore is beneficial to the elimination of azimuthal non-uniformity. It is important to note that, the geometries discussed in this work represent typical dimensions used in industry and may be considered as a base case. The multiscale model developed here may be easily modified to fit specific PECVD reactor schematics provided by a given manufacturer.

The net effect of the adjusted showerhead geometry on spatial uniformity is reflected in Fig. 14b, where the concentration of SiH_3 in cells bordering the substrate surface show significantly improved uniformity. When compared to the cross section in Fig. 14a, the adjusted reactor design has virtually eliminated 'hot spots' or regions of high SiH_3 concentration. More specifically, in Fig. 15a the reduction in x_{SiH_3} variation for fixed radial positions is obvious (i.e., the black circles as compared to the red triangles). As discussed previously, uniformity of the thin film product thickness is of greater interest than species concentration alone. To that end, the circular and triangular data points in Fig. 15b demonstrate that the *a*-Si:H thickness offset has been reduced from $\sim$25 nm to less than 13 nm near the edge of the substrate at the completion of the batch deposition process. The regions beyond $r = 8$ cm in Fig. 15 denote the exit port of the PECVD reactor. As shown in Figs. 1 and 13, these regions lie beyond the wafer substrate and therefore no film thickness data exits and the slight increase in SiH_3 concentration cannot affect film growth.
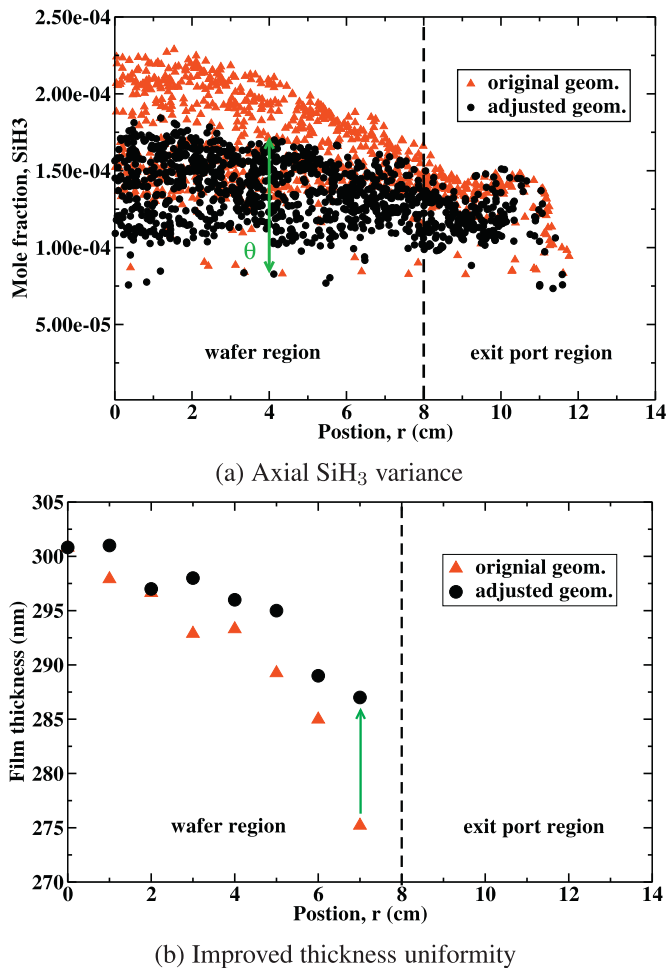
(a) Axial SiH$_3$ variance

(b) Improved thickness uniformity

Fig. 15. (a) SiH$_3$ mole fraction as a function of radial position, r, and azimuthal position, θ. (b) Radial a-Si:H product thickness for both the original and adjusted reactor geometries. (For interpretation of the references to color in this figure, the reader is referred to the web version of this article.)

4. Conclusions

An alternative PECVD reactor design has been evaluated using a three-dimensional multiscale CFD model which coordinates communication between the macroscopic reactor scale and the microscopic thin film growth domain. Application of this model to two representative PECVD reactor geometries has shown that thickness non-uniformity in the a-Si:H product can be minimized by adjusting the positions and size of the showerhead holes. As a result, the 3D CFD model presented holds promise for not only improving product quality in PECVD processing, but also for significant

savings in time and resources otherwise spent on the testing and manufacture of physical reaction chambers.

References

ANSYS Inc., 2013. ANSYS Fluent Theory Guide 15.0 (November).

Bakos, T., Valipa, M., Maroudas, D., 2005. Thermally activated mechanisms of hydrogen abstraction by growth precursors during plasma deposition of silicon thin films. J. Chem. Phys. 122, 1–10.

Bakos, T., Valipa, M., Maroudas, D., 2006. First-principles theoretical analysis of silyl radical diffusion on silicon surfaces. J. Chem. Phys. 125, 1–9.

Cheimarios, N., Kokkoris, G., Boudouvis, A., 2016. A multi-parallel multiscale computational framework for chemical vapor deposition processes. J. Comput. Sci. 15, 81–85.

Collins, D., Strojwas, A., White, D., 1994. A CFD model for the PECVD of silicon nitride. IEEE Trans. Semicond. Manuf. 7, 176–183.

Crose, M., Kwon, JSI., Nayhouse, M., Ni, D., Christofides, P.D., 2015. Multiscale modeling and operation of PECVD of thin film solar cells. Chem. Eng. Sci. 136, 50–61.

Crose, M., Kwon, JSI., Tran, A., Christofides, P.D., 2017a. Multiscale modeling and run-to-run control of PECVD of thin film solar cells. Renewable Energy 100, 129–140.

Crose, M., Tran, A., Christofides, P.D., 2017b. Multiscale computational fluid dynamics: methodology and application to PECVD of thin film solar cells. Coatings 7, 23.

Culler, D., Singh, J., Gupta, A., 1999. Parallel Computer Architecture: A Hardware/Software Approach. Gulf Professional Publishing.

da Silva, A., Morimoto, N., 2002. Gas flow simulation in a PECVD reactor. In: Proceedings of the International Conference on Computational Nanoscience and Nanotechnology, pp. 22–25.

Economou, D., Park, S., Williams, D., 1989. Uniformity of etching in parallel plate plasma reactors. J Electrochem Soc 136, 188–198.

Gerogiorgis, D., Ydstie, B., 2005. Multiphysics CFD modelling for design and simulation of a multiphase chemical reactor. Chem. Eng. Res. Des. 83, 603–610.

Ingle, N., Mountziaris, T., 1995. A multifrontal algorithm for the solution of large systems of equations using network-based parallel computing. Comput. Chem. Eng. 19, 671–681.

Kushner, M., 1988. A model for the discharge kinetics and plasma chemistry during plasma enhanced chemical vapor deposition of amorphous silicon. J. Appl. Phys. 63, 2532–2551.

Kwon, JSI., Nayhouse, M., Christofides, P.D., 2015. Multiscale, multidomain modeling and parallel computation: application to crystal shape evolution in crystallization. Ind. Eng. Chem. Res. 54, 11903–11914.

Nakano, A., Bachlechner, M., Kalia, R., Lidorikis, E., Vashishta, P., Voyiadjis, G., Campbell, T., Ogata, S., Shimojo, F., 2001. Multiscale simulation of nanosystems. Comput. Sci. Eng. 3, 56–66.

Park, S., Economou, D., 1991. A mathematical model for etching of silicon using CF$_4$ in a radial flow plasma reactor. J. Electrochem. Soc. 138, 1499–1508.

Perrin, J., Shiratani, M., Kae-Nune, P., Videlot, H., Jolly, J., Guillon, J., 1998. Surface reaction probabilities and kinetics of H, SiH$_3$, Si$_2$H$_5$, CH$_3$, and C$_2$H$_5$ during deposition of a-Si:H and a-C:H from H$_2$, SiH$_4$, and CH$_4$ discharges. J. Vac. Sci. Technol. A 16, 278–289.

Rasoulian, S., Ricardez-Sandoval, L., 2014. Uncertainty analysis and robust optimization of multiscale process systems with application to epitaxial thin film growth. Chem. Eng. Sci. 116, 590–600.

Rasoulian, S., Ricardez-Sandoval, L., 2015. A robust nonlinear model predictive controller for a multiscale thin film deposition process. Chem. Eng. Sci. 136, 38–49.

Robertson, J., 2000. Deposition mechanism of hydrogenated amorphous silicon. J. Appl. Phys. 87 (5), 2608–2617.